Progress In Electromagnetics Research C, Vol. 123, 263–279, 2022

A Wideband Polarization Conversion Coding Metasurface for Monostatic Radar Cross Section Reduction of High Altitude Aerospace Platforms

E. V. Bhavya[1, 2], Balamati Choudhury[1, *], and Raveendranath U. Nair[1]

Abstract—A novel wideband cross-polarized coding metasurface has been presented in this paper towards reduction of monostatic radar cross section (RCS). A broadband reflective cross-polarization converter for linearly polarized (LP) electromagnetic waves covering both X and Ku bands has been designed for this purpose. The proposed unit cell is ultrathin ($\lambda/15.7$) and demonstrates a polarization conversion bandwidth of 10.84 GHz from 7.96 GHz to 18.8 GHz for a linearly polarized normal incidence wave which helps in the reduction of radar cross section. In order to have a better understanding of cross polarization conversion (CPC), the physical mechanism of the structure has been investigated and elucidated in detail, along with the surface current distribution. The proposed structure has been studied for both transverse electric (TE) and transverse magnetic (TM) polarizations. For 1-bit coding, the suggested unit cell is utilized as the '0' bit, while the 90° rotated version of the unit cell is used as the '1' bit. A 4×4 matrix is built, and 16 configurations are explored. These combinations are known as the 2×2 metasurface sub-blocks, and they are used to build 200×200 components with size of 180 mm × 180 mm. The RCS simulation studies have been carried out from 2 to 30 GHz, and the proposed design shows a 10 dB RCS reduction from 10 GHz to 20 GHz. The scattering pattern of the suggested metasurface is comprehensively analyzed at 10 GHz, 15 GHz, and 18 GHz and demonstrates diffuse scattering in the other direction, minimizing the forward scattering RCS. The designed structure of 2.4 mm thickness has been fabricated and measured in the X- and Ku-bands. The measured results are in good agreement with simulated ones. In order to show the efficiency of the proposed coding metasurface, monostatic RCS estimation of the wing and body sections of high altitude aerospace paltforms (HAPS) has been simulated, and a 14.32 dB reduction has been observed over the body cross section.

1. INTRODUCTION

Advances in artificially engineered materials, such as metamaterials/metasurface, have piqued the interest of the aerospace and strategic industries due to their unique electromagnetic properties in reducing the RCS of a complex object. Shaping, active loading, passive loading, and distributed loading can all be used to reduce the RCS of a complex object. Shaping works against monostatic radars by avoiding surfaces perpendicular to the incoming waves, causing reflected waves to travel in the opposite direction to the source. Passive loading uses resistive sheets to limit the scattering, whereas active loading uses jammers to reduce the RCS of the object. The radar cross section reduction (RCSR) techniques using metasurfaces can be divided into three groups based on their respective working principles, i.e., cloaking, scattering, and absorbing. High impedance metasurfaces are being developed

Received 27 April 2022, Accepted 11 July 2022, Scheduled 8 September 2022

* Corresponding author: Balamati Choudhury (balamati@nal.res.in).

[1] Centre for Electromagnetic Division, CSIR-National Aerospace Laboratories, Bangalore, Karnataka 560017, India. [2] Academy of Scientific and Innovative Research (AcSIR), Ghaziabad, Uttar Pradesh 201002, India.

to reduce the RCS of complex objects via diffuse scattering, while metamaterial structures are being investigated as absorbers.

Landy et al. created the first perfect metamaterials based microwave absorber, with an absorbance peak of more than 88% at 11.5 GHz [1]. Since then, much research has been conducted in the field of metamaterials-based microwave absorbers, and the quest for the perfect absorber has expanded from microwave to infrared and optical regions. The primary focus on microwave absorbers has been on developing perfect absorbers that are broadband, polarization independent, and angle independent, and obtaining a perfect absorber with all of these characteristics is a difficult task. Metamaterial absorbers are resonant absorbers; hence they lack wideband performance.

To get a wide band RCS reduction, phase gradient metasurface has been introduced where the RCSR is achieved by anomalous reflection/diffuse scattering. The main mechanism behind anomalous reflection is to reflect the incident energy in all other directions in order to limit backscattering, resulting in a low observable object. Traditionally this was done by shaping the surface of the object; however, this can be done using a sub-wavelength resonator by reshaping the EM wave through adjusting the geometrical positions or converting the polarization of reflected wave.

Sun et al. proposed a phase gradient metasurface in 2012 to couple spatially propagating waves into surface waves [2]. Because of its exceptional properties, this method was further extended to perfect absorbing materials in order to improve absorption while maintaining a low thickness. Giovampaola and Engheta developed digital metamaterials in 2014, which used metamaterials bits to construct metamaterials bytes [3]. Cui et al. first proposed the idea of coding metasurfaces the same year [4]. A sequence of binary coding particles "0" and "1" were used to create a 1-bit coding metasurface, which corresponds to "0" and "p" phase responses, respectively. Because of diffusion scattering, the backward RCS was significantly reduced by using 1-bit coding. Furthermore, the RCS can be reduced further by scattering the incident wave in other directions, which necessitates more phase changes. Cross polarization converter metasurfaces contribute significantly to the low-observation goal by reducing the backscattering RCS. As polarization independent phase gradient metasurfaces require symmetric resonators to manipulate the incident electromagnetic wave, the bandwidth of such structures is limited by symmetric resonators. In order to improve the bandwidth, asymmetric structures having ultra-wideband polarization conversion features can be used. Chen et al. demonstrated broadband anomalous refraction by using asymmetric linear polarization converters [5]. After that, a lot of research has been done in cross polarization converters to use in anomalous refraction to reduce the RCS [6–13].

For RCS reduction, a wideband cross-polarized coding metasurface is proposed in this paper. The proposed structure consists of a metal-backed single-dielectric substrate on which simple metallic patches have been imprinted. Simulation studies show a polarization conversion ratio (PCR) bandwidth of 10.84 GHz from 7.96 GHz to 18.8 GHz. Three polarization conversion peaks with PCRs of 0.999, 0.989, and 0.999 were achieved during simulation at 8.54 GHz, 13.17 GHz, and 18.1 GHz, respectively. The physical mechanism of cross polarization conversion has been presented in detail by analyzing the surface current distribution. The asymmetric cross polarization converter unit cell is used to design coding metasurfaces. For 1-bit coding, the proposed unit cell is used as the '0' bit, and the 90° rotated version of the unit cell is used as the '1' bit. A 4×4 matrix is created, and 16 configurations are considered. These combinations are identified as the 2×2 metasurfaces sub-blocks, and they are used to construct 200×200 elements with dimensions of 180 mm × 180 mm. The proposed design, when being simulated using CST microwave studio, results in a reduction in RCS with respect to perfect electric conductor(PEC) from 2 GHz to 30 GHz and 10 dB reduction from 10 GHz to 20 GHz. In order to verify the effectiveness of the coding metasurface for RCS reduction, simulations were performed to determine the monostatic RCS reduction of the coding metasurface over the wing and a portion of the body cross section of high altitude aerospace platforms.

2. DESIGN AND ANALYSIS OF THE STRUCTURE

2.1. Electromagnetic Design

Figure 1 depicts the unit cell of the proposed reflective cross polarization converter. An almond-shaped metallic pattern is printed on top of a metal backed dielectric substrate. An FR4 substrate ($\varepsilon_r = 4.3$ and $\tan\delta_e = 0.025$) of 2.4 mm thickness is used as the dielectric in the design, and 0.035 mm thick copper

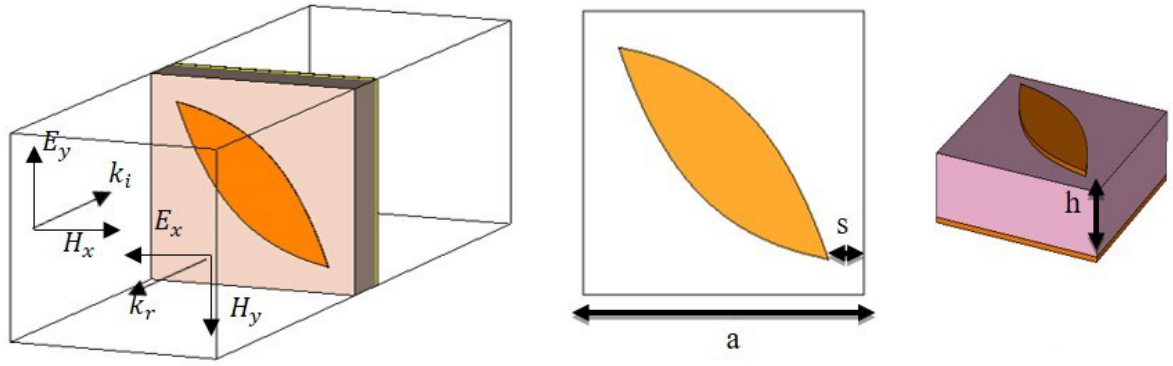

Figure 1. (a) Proposed unit cell design, (b) Top view ($a = 9\,\text{mm}$, $s = 1.145\,\text{mm}$), and (c) metamaterial unit cell ($h = 2.4\,\text{mm}$).

($\sigma = 5.8 \times 107\,\text{S/m}$) is used as the metal in the proposed design. An analytical exponential curve equation is used to design the structure, and the curvature is optimized for wideband performance. The geometrical parameters are optimized to achieve desirable characteristics, and the corresponding optimized dimensions are given in Figure 1. A metallic ground plane is incorporated into this design to improve the reflective cross polarization by limiting electromagnetic wave transmission and therefore increasing the cross-polarization conversion ratio. Using periodic boundary conditions and Floquet port excitation, simulation is performed to analyze the characteristics of the proposed structure using commercially available CST Microwave Studio software.

To comprehend the concept of cross polarization conversion, consider an X-polarized incident wave as,

$$\overrightarrow{E^i} = \hat{e_x^i} e^{j\left(-\overrightarrow{k^i}\cdot\overrightarrow{r}+\omega t\right)} \tag{1}$$

The reflected wave is denoted by

$$\overrightarrow{E^r} = \left(r_{xx}\hat{e_x^r} + r_{yx}\hat{e_y^r}\right) e^{j\left(-\overrightarrow{k^r}\cdot\overrightarrow{r}+\omega t\right)} \tag{2}$$

where $\hat{e_x^i}$ is the incident unit E vector along X-direction, $\hat{e_x^r}$ the reflected unit E vector along X-direction, and $\hat{e_y^r}$ the reflected unit E vector along Y-direction. Similarly, $\overrightarrow{k^i}$ and $\overrightarrow{k^r}$ are the wave vectors along incident and reflected direction. r_{xx} and r_{yx} represent the reflection coefficients of X-to-X and X-to-Y polarization components. Similarly, for a Y-polarized incident wave,

$$\overrightarrow{E^i} = \hat{e_y^i} e^{j\left(-\overrightarrow{k^i}\cdot\overrightarrow{r}+\omega t\right)}. \tag{3}$$

$$\overrightarrow{E^r} = \left(r_{yy}\hat{e_y^r} + r_{xy}\hat{e_x^r}\right) e^{j\left(-\overrightarrow{k^r}\cdot\overrightarrow{r}+\omega t\right)}, \tag{4}$$

where $\hat{e_y^i}$ is the incident unit E vector along Y-direction, $\hat{e_y^r}$ the reflected unit E vector along Y-direction, and $\hat{e_x^r}$ the reflected unit E vector along X-direction. Similarly, $\overrightarrow{k^i}$ and $\overrightarrow{k^r}$ are the wave vectors along incident and reflected direction. The co-polarization and cross-polarization reflection coefficients are represented by r_{yy} and r_{xy}, respectively. Simulated reflection characteristics of the proposed unit cell are shown in Figure 2. The structure is analyzed for both TE and TM polarizations for a normally incident electromagnetic wave and are shown in Figure 2(a) and Figure 2(b). Figure 2 shows that cross polarization reflection is greater for both TE and TM polarized incident waves than co-polarization reflection. PCR for a Y-polarized incident wave can be defined as

$$PCR = \frac{{r_{xy}}^2}{{r_{yy}}^2 + {r_{xy}}^2}. \tag{5}$$

The PCR of the structure over its entire operating range has been computed and plotted using Equation (5) (as shown in Figure 3(a)). A cross polarization conversion ratio of 70% is maintained by cross-polarized reflection coefficients larger than -3 dB ($r_{yx} > -3$ dB and $r_{xy} > -3$ dB) and co-polarized reflection coefficients less than -6 dB ($r_{xx} < -6$ dB and $r_{yy} < -6$ dB). However, if the cross-polarization efficiency exceeds 90%, the magnitude of co-polarized refection coefficients should be less than -10 dB ($r_{xx} < -10$ dB and $r_{yy} < -10$ dB), and cross-polarized refection coefficients should be larger than -2 dB ($r_{yx} > -2$ dB and $r_{xy} > -2$ dB). For the proposed structure, a cross-polarization coefficient larger than -2 dB and co-polarized coefficient less than -10 dB are achieved for both TE and TM polarizations as shown in Figure 2(a) and Figure 2(b). Within the operating region, a PCR bandwidth of 10.84 GHz is obtained for both TE and TM polarizations, as shown in Figure 3(a). Hence, the structure converts the polarization of an X-polarized wave to a Y-polarized wave and back. The cross-polarization is the

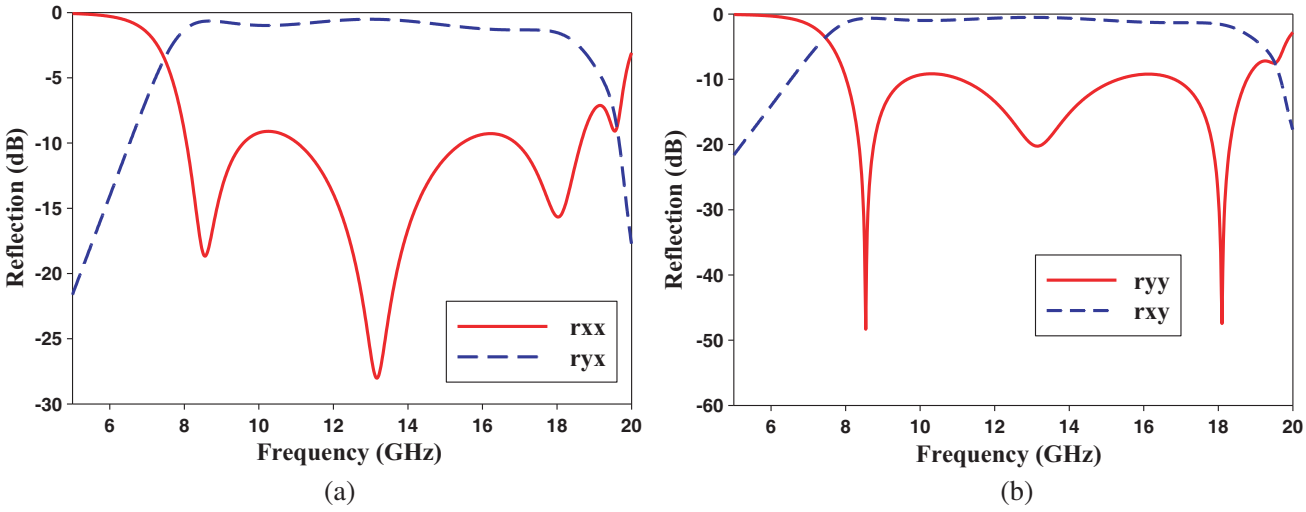

Figure 2. Reflection characteristics of proposed structure. (a) Co-polarized and cross-polarized reflections in dB for an X-polarized incident wave, and (b) Co-polarized and cross-polarized reflections in dB for Y-polarized incident wave.

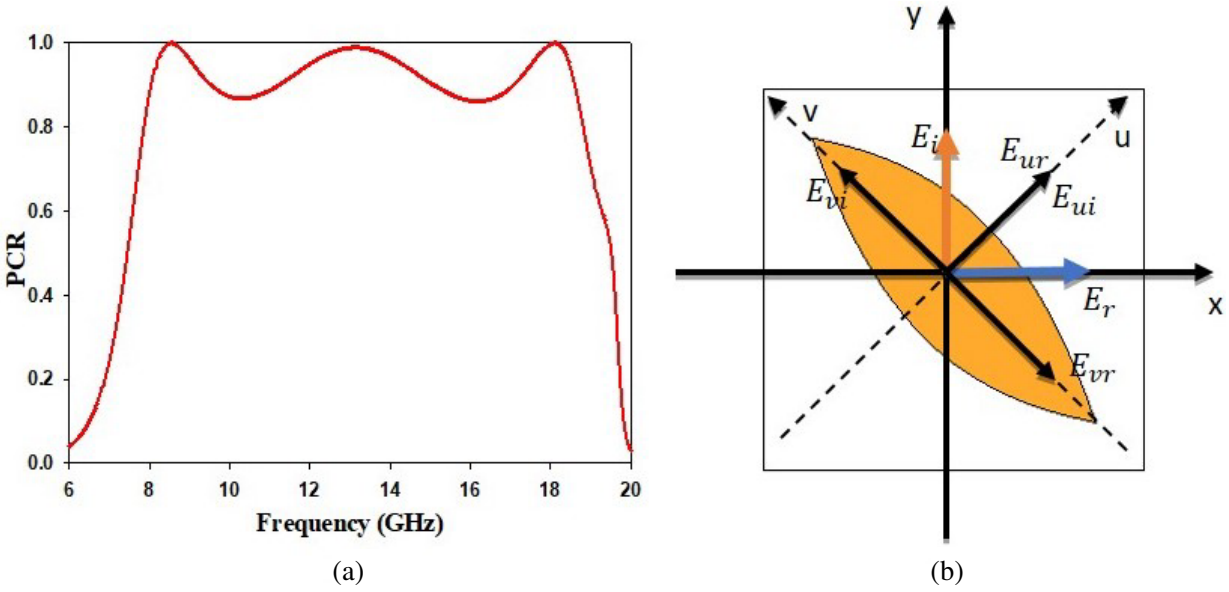

Figure 3. (a) PCR for the proposed CPC structure, and (b) Illustration of polarization conversion from Y- to X-polarization.

greatest at three separate resonance frequencies. The first happens at 8.54 GHz, while the second and third occur at 13.17 GHz and 18.1 GHz, respectively.

2.2. Physical Mechanism

The designed structure is an asymmetric structure with asymmetry along both the X- and Y-axes. However, the structure is symmetric along the U- and V-axes, which are at a $\pm 45^\circ$ angle with respect to the Y-axis, as illustrated in Figure 3(b). Simulation studies for both U- and V-polarizations have been carried out to investigate the physical mechanism underlying cross-polarization conversion. Asymmetry along X- and Y-axes in the structure introduces an anisotropy in the structure, hence the proposed structure can be regarded as an anisotropic homogeneous metamaterial with a relative permeability tensor ($\overrightarrow{\mu_r}$) and a relative permittivity tensor ($\overrightarrow{\epsilon_r}$), in which the anisotropic axis is designated by the U-, V-, and Z-axes. Since the structure has a symmetry along U- and V-axes, cross-polarized components of the reflected electromagnetic wave will not exist at U-polarized and V-polarized incidences [13]. To understand the physical mechanism of the cross-polarization conversion, a Y-polarized wave at normal incidence is considered, and the Y-polarized wave is decomposed into U-polarized and V-polarized components, as illustrated in Figure 3(b). From Figure 3(b), the incident electric field vector $\overrightarrow{E^i}$ and reflected field vector $\overrightarrow{E^r}$ can be denoted as

$$\vec{E^i} = E_{yi}\hat{e_y} = E_{ui}\hat{e_u} + E_{vi}\hat{e_v} = E_{yi}\cos 45^\circ\left(\hat{e_u} + \hat{e_v}\right) \tag{6}$$

$$\begin{aligned}\vec{E^r} &= E_{ur}\hat{e_u} + E_{vr}\hat{e_v} = r_u E_{ui}\hat{e_u} + r_v E_{vi}\hat{e_v} \\ &= E_{yi}\cos 45^\circ(r_u\hat{e_u} + r_v\hat{e_v})\end{aligned} \tag{7}$$

where $\hat{e_u}$ and $\hat{e_v}$ denote the unit vectors in the U- and V-axes, and r_u and r_v denote the U-polarized and V-polarized reflection coefficients, respectively. A phase difference, $\Delta\varphi$, can be defined between r_u and r_v, thus

$$r_v = r_u e^{j\Delta\varphi} \tag{8}$$

Hence,

$$\vec{E^r} = r_u E_{yi}\cos 45^\circ\left(\hat{e_u} + e^{j\Delta\varphi}\hat{e_v}\right) \tag{9}$$

and the corresponding r_{xy} and r_{yy} can be determined as follows:

$$r_{xy} = \frac{|E_{xr}|}{|E_{yi}|} = \sqrt{(1-\cos\Delta\varphi)/2} \tag{10}$$

$$r_{yy} = \frac{|E_{yr}|}{|E_{yi}|} = \sqrt{(1+\cos\Delta\varphi)/2} \tag{11}$$

The phase difference $\Delta\varphi$ can be varied from -180° to $+180^\circ$ based on the operating frequency. Consequently, the axial ratio may be used to explain the polarization, and for an elliptical polarization, the axial ratio is equal to

$$AR = \sqrt{\frac{(1-\cos\Delta\varphi)/2}{(1+\cos\Delta\varphi)/2}} \tag{12}$$

According to Equation (11), all the polarizations including elliptical, linear, and circular ones can be achieved. When $\Delta\varphi = 90^\circ$, the axial ratio is 1, which indicates that the incident wave has been converted into a circularly polarized wave. When $\Delta\varphi = 0^\circ$, $r_{xy} = 0$ and $r_{yy} = 1$, i.e., the incident wave is reflected back without any polarization conversion. When $\Delta\varphi = 180^\circ$, $r_{xy} = 1$ and $r_{yy} = 0$, resulting in a 90° polarization rotation, as shown in Figure 3(b). Simulations were carried out to investigate the designed structure's cross-polarization conversion, as illustrated in Figure 4. Figure 4(a) demonstrates that the simulated magnitudes of r_u and r_v in the operating frequency are both substantially closer to 0 dB, satisfying the cross-polarization conversion condition. Although there is a small difference between r_u and r_v, this is due to the FR4 substrate's dielectric loss. From 8 GHz to 18.9 GHz, the phase differences $\Delta\varphi$ between the reflection coefficients of u and v polarized waves are close to 180°, as illustrated in Figure 4(b). Also, at the frequencies of 8.21 GHz, 8.58 GHz, 13.2 GHz, and 18.1 GHz, $\Delta\varphi$ is exactly equal

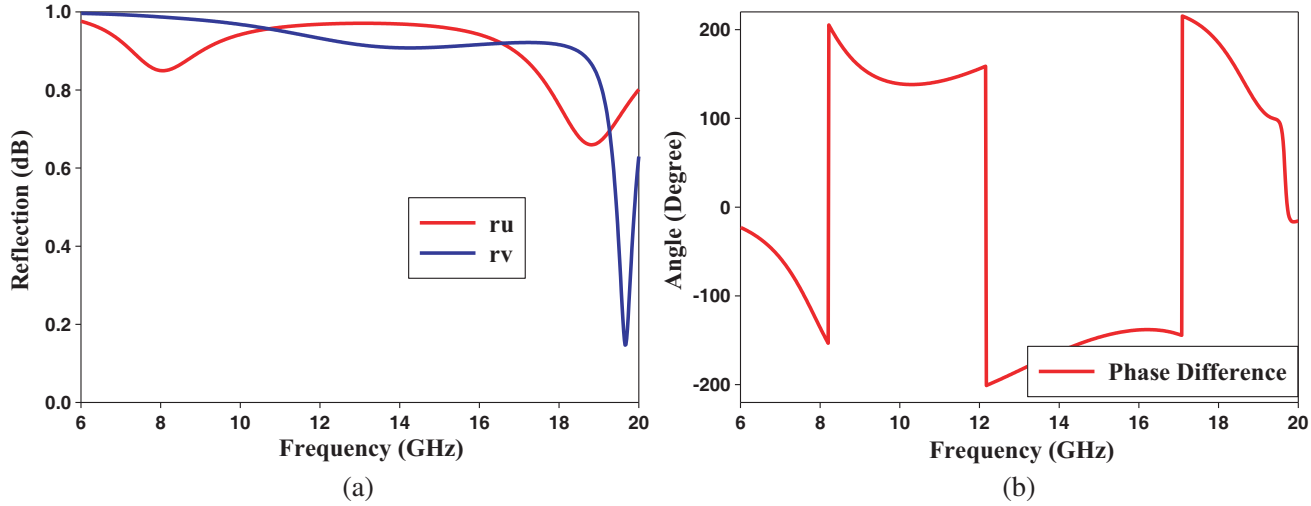

Figure 4. (a) Reflection for U- and V-polarized incidence, and (b) phase difference between the U- and V-polarized wave.

to 180°, which is nearly identical to the three plasmon resonance frequencies (8.54 GHz, 13.17 GHz, and 18.1 GHz) in Figure 2(a). Finally, it can be concluded that the cross-polarization conversion is caused by the anisotropy of the unit cell structure, which acts as a half wave plate, converting the X-polarized wave to the Y-polarized wave and vice versa.

It is also worth noting that the co-polarized reflection is considerable for U- and V-polarized waves, as shown in Figure 4. As a result, cross polarization conversion for waves polarized along symmetric axes (U- and V-axes) is not possible with the proposed design. In reality, the anisotropy of the proposed structure causes cross polarization conversion, which means that X-polarized waves are transformed to Y-polarized waves and Y-polarized waves transformed into X-polarized waves, i.e., the polarization converter converts the wave only into its orthogonal polarization.

Cross-polarization conversion can also be studied by looking at the surface current distribution on the unit cell's top patch and bottom ground plane at resonant frequencies. Figure 5 displays the

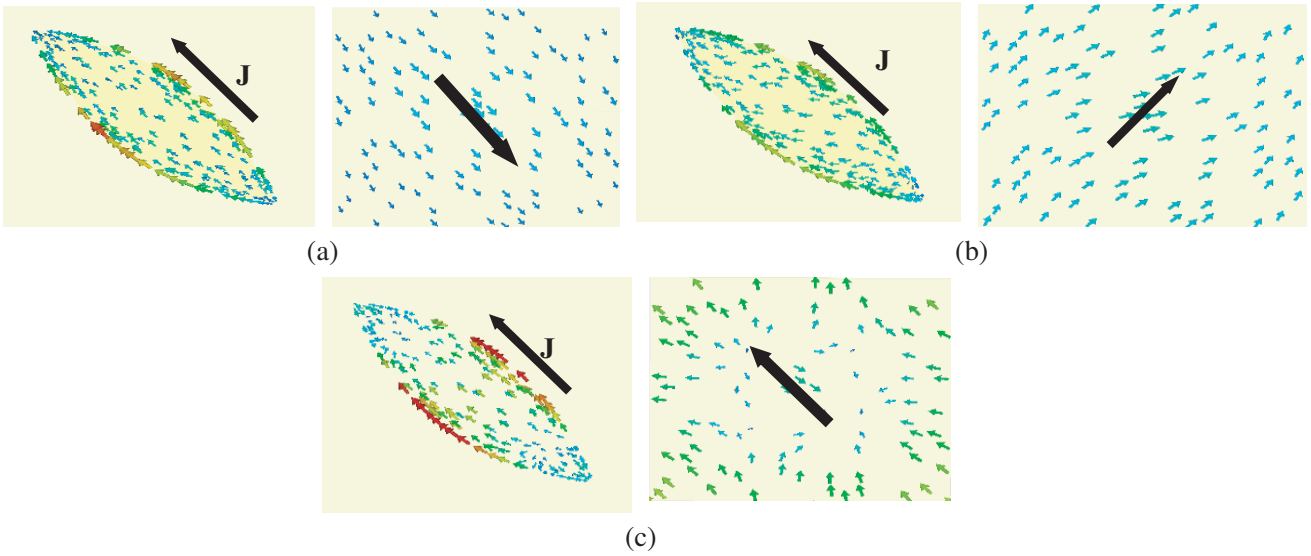

Figure 5. Surface current distribution at the resonance frequencies, (a) at 8.54 GHz, (b) at 13.17 GHz, and (c) at 18.1 GHz.

surface current distributions over the designed structure's top and bottom metallic layers at resonance frequencies of 8.54 GHz, 13.17 GHz, and 18.1 GHz. When an electromagnetic wave with E polarization vector along Y-axis is incident on the structure, electromagnetic responses are induced due to the coupling between the top metallic patch and bottom metal ground plane, causing the surface current to flow in opposing directions, according to Faraday's law. The currents in various sections of the proposed structure combine to form a resultant current, which is equal to the vector sum of the currents in the top and bottom layers. In Figure 5, the arrow with letter $\vec{J}$ represents the resultant current.

As illustrated in Figure 5(a), the resultant current $\vec{J}$ on the patterned layer and ground plane is flowing in opposite directions at 8.54 GHz, resulting in magnetic resonance. Figure 5(b) shows an identical mechanism at the resonance frequency of 13.17 GHz. An electric resonance can be observed at 18.1 GHz because the net electric current in the top patterned and bottom metallic layers is flowing in the same direction as shown in Figure 5(c). Significant electromagnetic response is produced as a result of the electric and magnetic resonances induced in the structure. The co-polarization reflection is significantly reduced as a result of these effects, whereas the cross-polarization reflection increases, enhancing the structure's PCR.

2.3. Oblique Incidence

The proposed structure is studied for oblique incidences under both TE and TM polarizations. Figure 6 shows the simulated PCR for the two cases of TM and TE polarizations at various incidence angles (θ), and it can be observed that the oblique incidence has an influence on the polarization conversion bandwidth. Once θ is gradually incremented from 0° to 30°, the PCR is decreased, which is shown in Figure 6. At higher frequencies, cross polarization conversion diminishes for different incidence angles (θ). For an oblique incidence, the propagation phase (βd) can be calculated as

$$4\beta d = \frac{4\sqrt{\varepsilon_r}k_0 h}{\cos\theta_i} \tag{13}$$

where θ_i is the incidence angle. From this equation, it can be noted that the propagation phase is higher than that of normal incidence case. The higher propagation phase causes destructive interference at CPC structure surfaces and limits cross-polarization conversion bandwidth. At higher frequencies, as the incidence angle θ is increased, the propagation phase fluctuates even more dramatically. A simulation has been done to analyze the oblique incidence on CPC structure for both TE and TM polarizations.

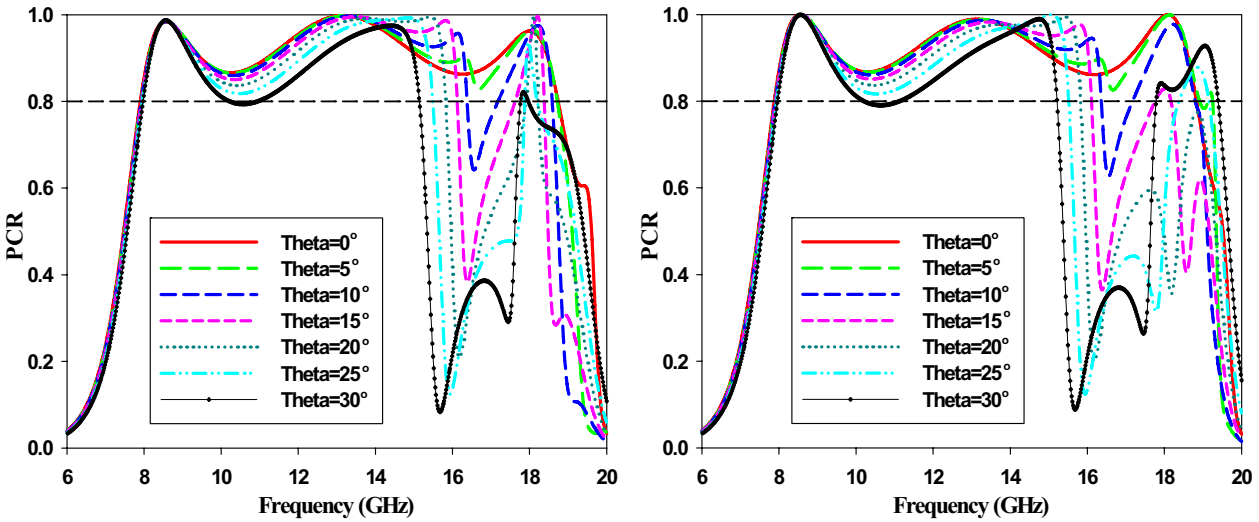

Figure 6. (a) PCR of Y-polarized wave at oblique incidence, and (b) PCR of X-polarized wave at oblique incidence.

When incidence angle (θ) is raised from 0° to 30° with a step size of 5°, the PCR bandwidth drops from 10.84 GHz to 8 GHz, with a conversion efficiency of more than 80%.

Table 1 compares the proposed work to other broadband cross polarization converters published previously. The comparison shows that the proposed wideband reflective metasurface cross polarization converter has a broadband property, with a PCR bandwidth of more than 81% and a lower thickness of $\lambda/15.7$ in relation to the lowest frequency of operation, implying excellent performance with a lower thickness. Because there is always a trade-off between high performance and thickness, this design provides an optimized cross polarization converter with wide band performance and lower thickness in X and Ku bands than other published works.

Table 1. Comparison with previously reported works.

Reference	Frequency band (GHz)	Relative PCR B. W. (%)	Thickness (mm)	Relative Thickness
[14]	6.9–15.4	76	3	$\lambda/14.49$
[15]	6.91–14.31	70	3	$\lambda/14.47$
[16]	9.4–19.2	69	3	$\lambda/10.64$
[17]	8.3–14.3	53	3	$\lambda/12.05$
[18]	7.6–15.5	68	3	$\lambda/13.16$
[19]	8–13.5	51	3.2	$\lambda/11.72$
[20]	8.1–14.6	57	2	$\lambda/18.52$
[21]	13–26	67	1.6	$\lambda/14.42$
[Present Study]	7.96–18.8	81	2.4	$\lambda/15.70$

3. CODING METASURFACE DESIGN

The antenna array theory can be used to explain the RCS reduction technique in the coding metasurface. Similar to an antenna array, each coding metasurface unit is treated as a dipole source, and the far field scattering characteristics are estimated by employing superposition and interference theory of EM waves on the coding metasurface units. To achieve the goal of RCS reduction, the metasurface is built in such a way that the EM waves are scattered in multiple directions, creating nonuniform and disordered scattering waves of very minimal energy. Because the energy in coding metasurface is redirected rather than absorbed, it does not raise the IR signature like traditional radar absorbers.

The proposed unit cell of reflective polarization converter can be used as coding metasurface to change the scattering parameters of the incident electromagnetic wave. A coding metasurfaces is designed using the above-mentioned unit cell. As shown in Figure 7(a), the proposed unit cell is used as the '0' bit for 1-bit coding, and the 90° rotated version of the unit cell is used as the '1' bit. The proposed unit cell's reflection properties have been investigated for both X- and Ku-bands, and the results for x-polarized and y-polarized incident waves are shown in Figure 2. The reflective polarization converter has a polarization conversion bandwidth of 10.84 GHz for both elements, as shown in Figures 2(a) and (b), spanning the frequency range of 7.96 GHz to 18.8 GHz. Consequently, the phases for both the elements are shown in Figure 7(b), and the phase difference is shown in Figure 7(c). Throughout the operational band, the phase difference between the two elements is 180°, allowing for phase cancellation. Since the '1' element is the rotated version of the original unit cell, the reflection properties of this element for an x-polarized wave are the same as the reflection properties of '0' element for a y-polarized wave and vice versa. As discussed above, the reflection properties of '0' element and '1' element are same but are out of phase. Hence, this property can be used to reduce the RCS of the structure through phase cancellation.

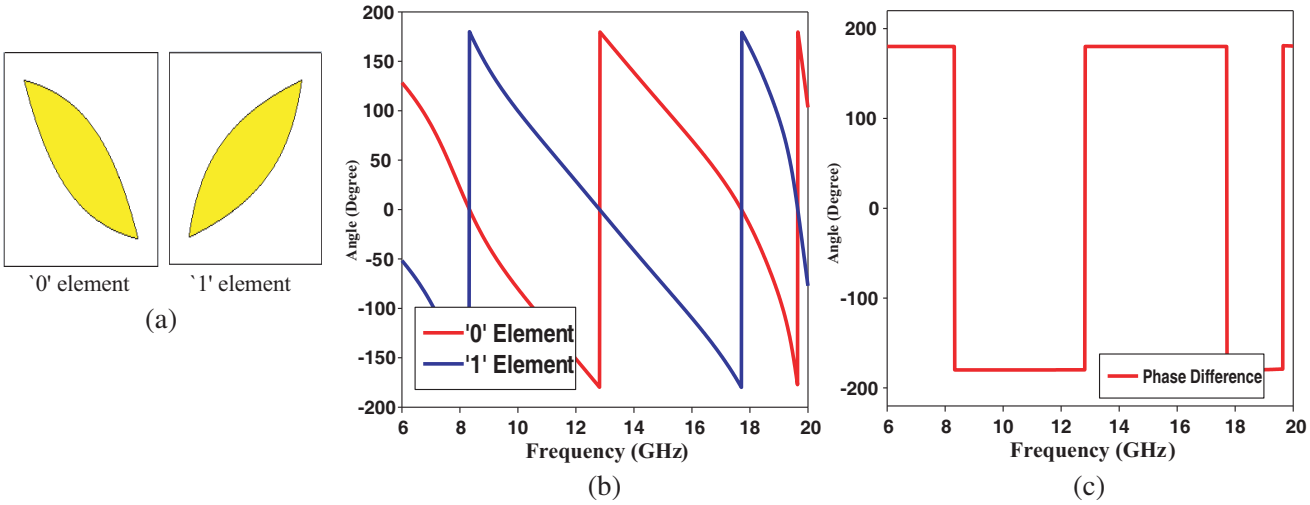

Figure 7. (a) Top view of the '0' element, (b) Top view of the '1' element, (c) Phase in degrees for '0' and '1' elements, and (d) Phase difference between two elements.

A 4×4 matrix is formulated for 1-bit coding, and 16 configurations are considered, with some of the elements repeating, so the redundant elements are omitted from the final formulation. Nine of the 16 available configurations were deemed redundant, and the remaining seven were chosen for simulation. The 4×4 matrix formulations are shown in Table 2. These seven configurations namely 0000, 0001, 0011, 0101, 0110, 0111, and 1111 are considered as the 2×2 metasurfaces sub-blocks, and they are used to build 200×200 elements with dimensions of 180 mm $\times$ 180 mm. The structure's monostatic RCS is determined by analyzing these 7 combinations with CST microwave studio. The available 7 combinations were used to simulate the monostatic RCS, and the results for horizontal polarization for a 180 mm $\times$ 180 mm plate are shown in Figure 8. To compare the result, monostatic RCS of a metal plate with same dimension has been simulated and shown in Figure 8(a). Out of these 7 combinations, all combinations show a reduced monostatic RCS from 2 GHz to 30 GHz, and in particular one combination shows reduced RCS compared to other six combinations. The combination 0101 shows a better RCS reduction than other combinations, and the results with respect to the RCS reduction are shown in Figure 8(b). Monostatic RCS for these 7 combinations in vertical polarization is shown in Figure 9(a), and the monostatic RCS reduction with respect to metal plate of the same dimension is shown in Figure 9(b). A 10 dB reduction is obtained from 10 GHz to 20 GHz for both horizontal and vertical polarizations for these combinations. With a 17.23 dB reduction, the maximum reduction appears at 15 GHz for 0101 combinations. The 2D and 3D far field scattering patterns of coding metasurface for X polarized wave are estimated at 10 GHz, 15 GHz, and 18 GHz. The 3D scattering pattern of a planar coding metasurface under normal incidence for an X polarized wave is shown in Figure 10. At 10 GHz, 15 GHz, and 18 GHz, the grating lobes are reduced, and the scattering field distribution is scattered into various regions. These patterns are then compared to a bare metallic plate of the same size, and it is demonstrated that compared to the bare metallic plate, the scattering fields of the coding metasurface are reallocated to the other directions, minimizing the RCS. At 10 GHz, 15 GHz, and 18 GHz, Figure 11

Table 2. Coding metasurface 4×4 formulation.

0/1	00	01	10	11
00	0000	0001	0010	0011
01	0100	0101	0110	0111
10	1000	1001	1010	1011
11	1100	1101	1110	1111

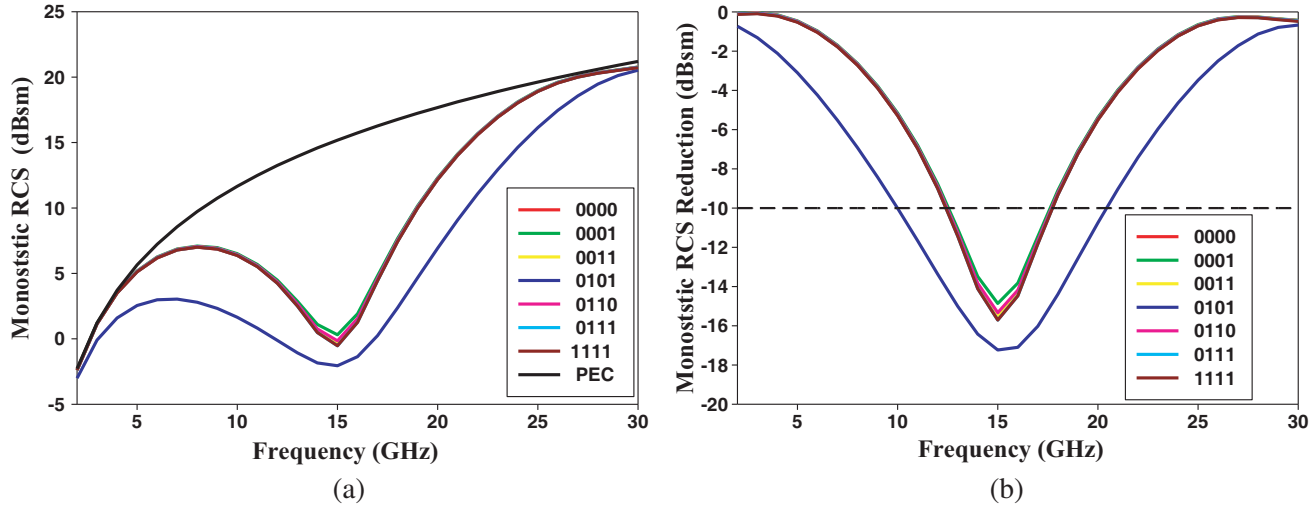

Figure 8. (a) Monostatic RCS of the 7 combinations compared with PEC at normal incidence for horizontal polarization, and (b) monostatic RCS reduction of the 7 combinations compared with PEC at normal incidence for horizontal polarization.

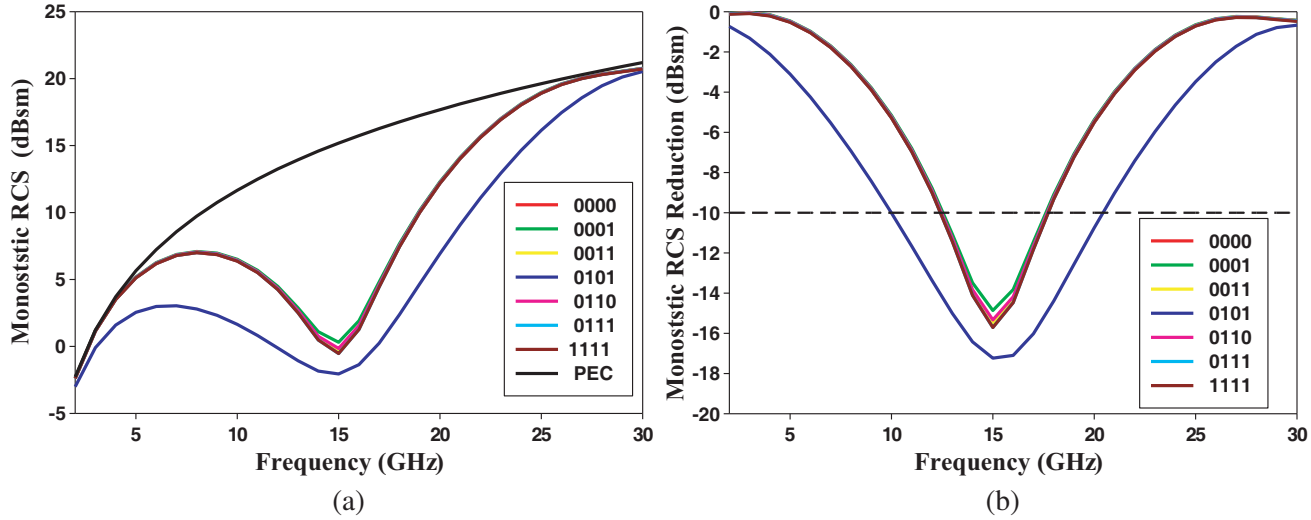

Figure 9. (a) Monostatic RCS of the 7 combinations compared with PEC at normal incidence for vertical polarization, and (b) monostatic RCS reduction of the 7 combinations compared with PEC at normal incidence for vertical polarization.

compares the 2D scattering patterns of the coding metasurface and bare metal plate.

The monostatic scattering of proposed coding metasurface is shown in Figure 11 for θ variation by keeping $\phi = 0°$. The Cartesian plot shows the monostatic scattering of proposed metasurface and reference metal plate at 10 GHz, 15 GHz, and 18 GHz, respectively. From Figure 11, it is shown that the total RCS of metasurface is far below for all the three frequencies compared to that of the PEC structure of the same dimension. At different incidence angles, the pattern starts to redistribute in other directions thereby reducing the total RCS of the structure.

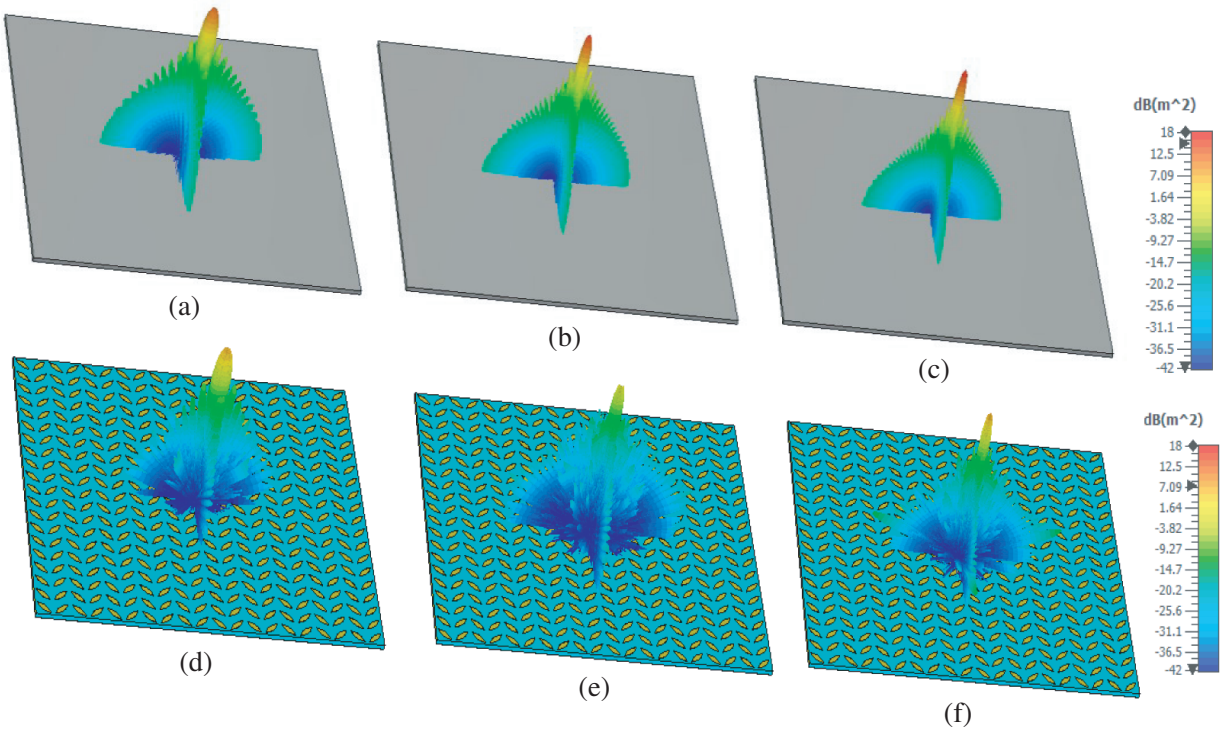

Figure 10. (a)–(c) 3D monostatic scattering of PEC at 10 GHz, 15 GHz and 18 GHz, and (d)–(f) 3D monostatic scattering of '0101' pattern at 10 GHz, 15 GHz, and 18 GHz.

4. SIMULATION OF CODING METASURFACE FOR HIGH ALTITUDE AEROSPACE PLATFORMS

The coding metasurface was designed to be utilized in high altitude platform systems in order to reduce the structure's RCS. The hotspots in HAPS were identified by simulation, and those hotspots were assumed to be covered with coding metasurface, as shown in Figure 12. The RCS analysis took into account the front end wing and a segment of body sections. These two pieces were coated with coding metasurface, and the RCS of these sections was estimated using CST Microwave Studio. Figure 13 depicts the 3D scattering of a cross section of a body portion, whereas Figure 14 depicts the scattering of a wing section. The 3D scattering of a portion of the HAPS body cross section has been compared to the metallic body cross section in Figure 13, and it has been shown that the scattering in the metallic body cross section is centered around the radial axis, whereas the energy in the coding metasurfaces coated cross section is redistributed to different directions, reducing the forward scattering. Figure 14 follows a similar response for the HAPS wing segment.

Figure 15 shows the monostatic scattering of the proposed coding metasurface coated HAPS body section for ϕ variation with $\theta = 90°$. Figure 15 shows that the total RCS of the metasurface coated structure is significantly lower for both frequencies than that of the bare metallic body cross-section of HAPS. At 10 GHz, normal incidence results in a 10.59 dB RCS reduction, while at 15 GHz, normal incidence results in a total of 14.32 dB RCS reduction. Figure 16 shows the monostatic scattering of the HAPS wing section for ϕ variation while maintaining $\theta = 90°$. At 10 GHz, the Cartesian plot reveals a 5.31 dB RCS reduction, while at 15 GHz, it shows a 7.3 dB RCS reduction.

5. FABRICATION AND MEASUREMENT

The proposed metasurface was fabricated on a 180 mm × 180 mm FR4 substrate with a dielectric constant of 4.3 and a thickness of 2.4 mm, using a prototype printer facility at Council of Scientific and Industrial

Research (CSIR)-National Aerospace Laboratories (NAL). On the front side of the substrate with a copper clad thickness of 35 µm, a total of 20 × 20 unit cells with an inter-element spacing of 2.29 mm were etched, with the bottom plate remaining as that with the copper coating as shown in Figure 17(d).

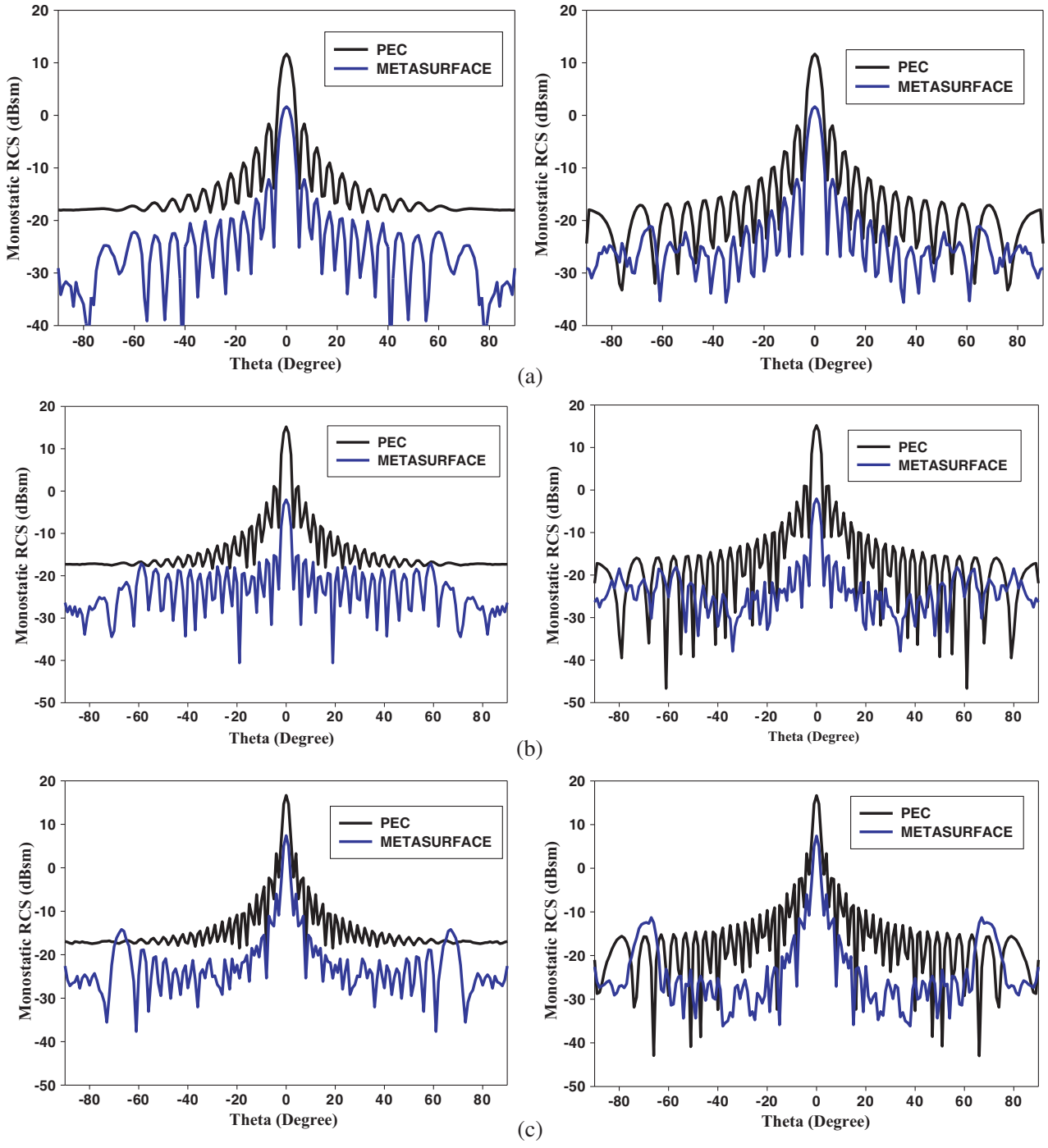

Figure 11. (a) Monostatic scattering of PEC and proposed metasurface at 10 GHz for both horizontal and vertical polarization for theta variation (at $\phi = 0°$), (b) monostatic scattering of PEC and proposed metasurface at 15 GHz for both horizontal and vertical polarization for theta variation (at $\phi = 0°$), and (c) monostatic scattering of PEC and proposed metasurface at 18 GHz for both horizontal and vertical polarization for theta variation (at $\phi = 0°$).

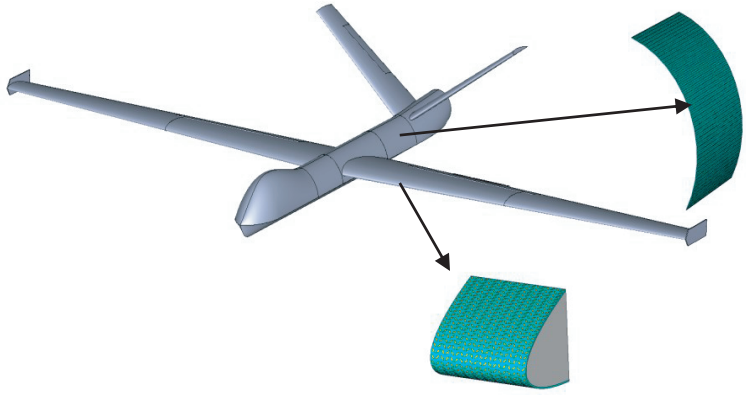

Figure 12. Representation schematic of HAPS with conformal coding metasurface.

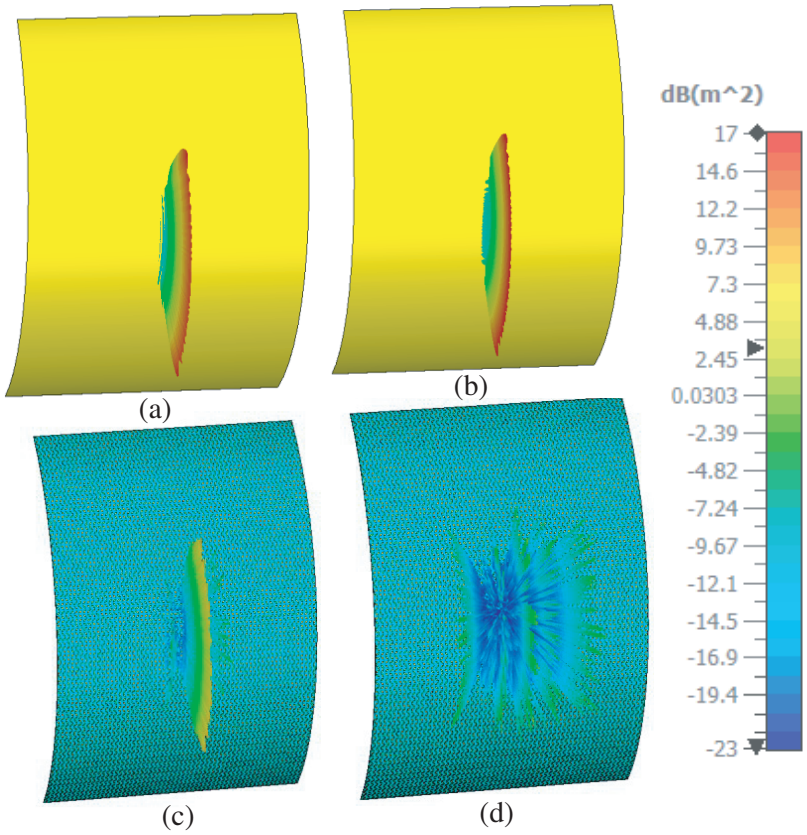

Figure 13. 3D scattering pattern of the cross section of HAPS body part with (a) bare metal at 10 GHz, (b) bare metal at 15 GHz, (c) coding metasurface at 10 GHz, and (d) coding metasurface at 15 GHz.

The fabrication has a three step procedure: (i) drilling, (ii) milling of the cu coating on an FR4 substrate, and (iii) routing of the whole structure from the substrate sheet.

Finally, the fabricated structure was measured in an anechoic room for the X- and Ku-bands, as illustrated in Figure 17(a). For the reflection measurement, two standard horn antennas operating in the 2–18 GHz band were utilized as the transmitter and receiver as illustrated in Figure 17(b). The

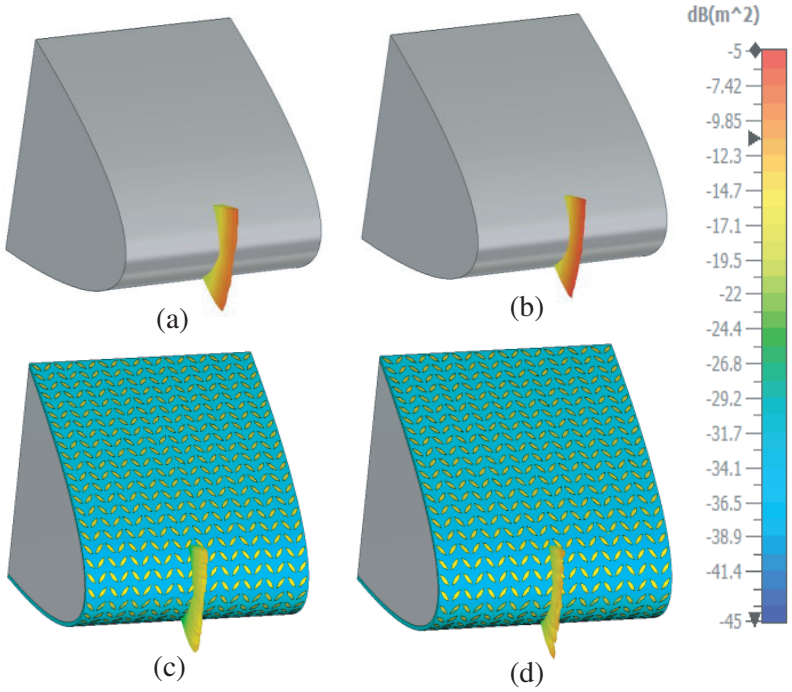

Figure 14. 3D scattering pattern of the cross section of HAPS wing with (a) bare metal at 10 GHz, (b) bare metal at 15 GHz, (c) coding metasurface at 10 GHz, and (d) coding metasurface at 15 GHz.

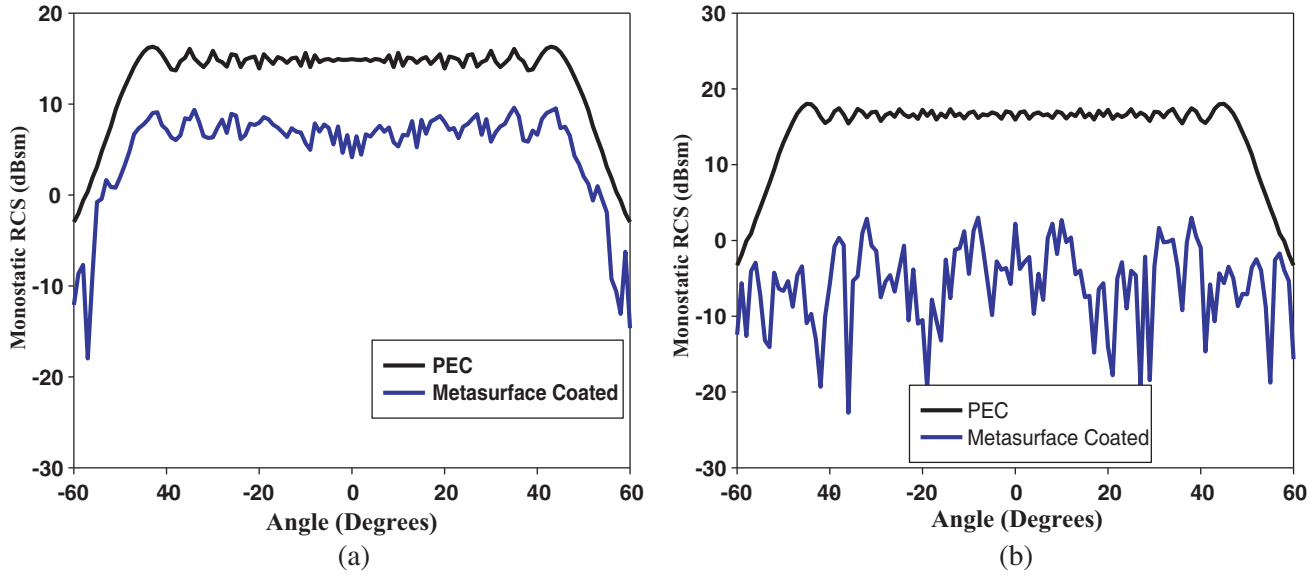

Figure 15. Monostatic RCS of bare metallic body cross section of HAPS and coding metasurface coated body cross section of HAPS for ϕ variation ($\theta = 90°$) at (a) 10 GHz for horizontal polarization, and (b) 15 GHz for horizontal polarization.

vector network analyzer (VNA) is calibrated using the conventional calibration technique, and the PCR structure is mounted on the platform, as illustrated in Figure 17(c). Both standard antennas are positioned on the same side, with one antenna linked to port 1 and the other to port 2. As a result, S_{21} is measured to assess the reflection property. After calibrating the VNA, measurement was

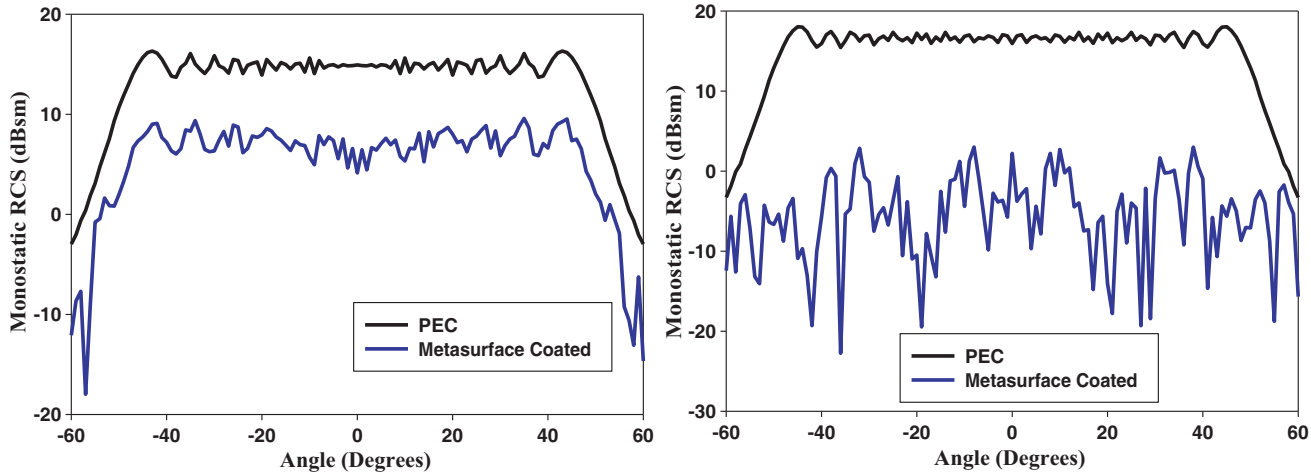

Figure 16. Monostatic RCS of bare metallic wing section of HAPS and coding metasurface coated wing section of HAPS for ϕ variation ($\theta = 90°$) at (a) 10 GHz for horizontal polarization, and (b) 15 GHz for horizontal polarization.

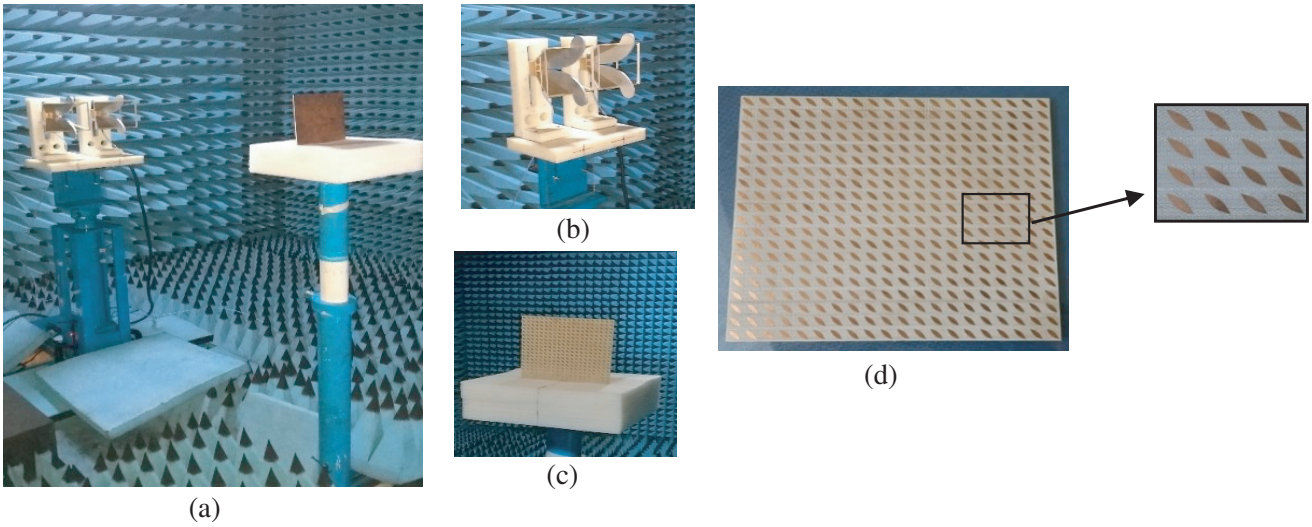

Figure 17. (a) Full measurement setup, (b) Antenna setup, (c) Fabricated structure setup, and (d) Fabricated PCR structure with a dimension of 180 mm × 180 mm.

performed without the structure to get background data, followed by a measurement of a metal plate measuring 180 mm × 180 mm as a standard sample. Subsequently, the S_{21} of the PCR structure was measured. In order to understand the cross-polarization reflection, both co-polarization and cross-polarization reflections have been measured. It is done by rotating the transmitting antenna to get cross-polarized wave, and the results are shown in Figure 18(a) and Figure 18(b) for both TE and TM polarizations. The reflection properties are obtained by considering the metal plate as the standard sample. Figure 18 shows that the measurement results are in good agreement with the simulation ones for both co-polarization and cross-polarization.

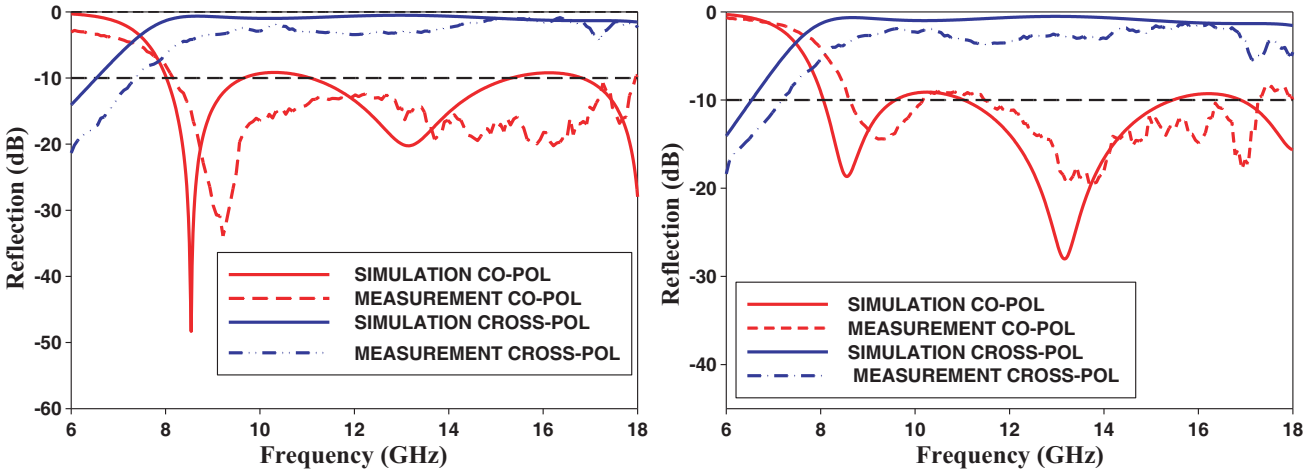

Figure 18. Measured and simulated co-polarization and cross-polarization reflection for (a) Y-polarized wave, and (b) X-polarized wave.

6. CONCLUSION

The design and development of a novel ultrathin cross polarization converter and its application in monostatic RCS reduction have been demonstrated in this work. The ultrathin cross polarization converter works in the operating range of 7.96 GHz–18.8 GHz with a bandwidth of 10.84 GHz. The structure has been studied for both TE and TM polarizations and angular dependencies. The physics behind the polarization conversion mechanism has been explained clearly with the help of surface current distribution mapping over the structure. A coding metasurface for RCS reduction via diffuse scattering is created utilizing the proposed linear cross polarization converter. The metasurface is created using 1-bit coding, with the cross-polarization converter unit cell acting as the '0' bit and 90° rotated version acting as the '1' bit. A 4×4 matrix is used to construct 2×2 sub-blocks, and these 2×2 blocks are used to create a 180 mm $\times$ 180 mm metasurface. The proposed metasurface is examined for scattering patterns at 10 GHz, 15 GHz, and 20 GHz and shows a 10 dB reduction in RCS compared to standard PEC structure from 10 GHz to 20 GHz. The polarization converter has been fabricated using a 3D printing technology and measured in an anechoic chamber. The measured results are in good agreement with the simulated ones. In order to demonstrate the efficacy of proposed coding metasurface in real-time application, a wing structure and a portion of the body cross section of an HAPS were investigated, and simulation tests were conducted in order to reduce RCS utilizing the proposed coding metasurface. For the normal incidence scenario, a 14.32 dB RCS reduction was observed for the HAPS body cross section, and a total of 7.3 dB RCS reduction was observed for the wing section.

ACKNOWLEDGMENT

Ms. Bhavya E. V. gratefully acknowledges the Department of Science and Technology (DST) of India for financial assistance provided under the INSPIRE Fellowship.

REFERENCES

1. Landy, N. I., S. Sajuyigbe, J. J. Mock, D. R. Smith, and W. J. Padilla, "Perfect metamaterial absorber," *Physical Review Letters*, Vol. 100, No. 20, 207402, 2008.
2. Sun, S., Q. He, S. Xiao, Q. Xu, X. Li, and L. Zhou, "Gradient-index meta-surfaces as a bridge linking propagating waves and surface waves," *Nature Materials*, Vol. 11, No. 5, 426–431, 2012.

3. Della Giovampaola, C. and N. Engheta, "Digital metamaterials," *Nature Materials*, Vol. 13, No. 12, 1115–1121, 2014.
4. Cui, T. J., M. Q. Qi, X. Wan, J. Zhao, and Q. Cheng, "Coding metamaterials, digital metamaterials and programmable metamaterials," *Light: Science & Applications*, Vol. 3, No. 10, e218–e218, 2014.
5. Chen, H., H. Ma, J. Wang, S. Qu, Y. Li, J. Wang, M. Yan, and Y. Pang, "A wideband deflected reflection based on multiple resonances," *Applied Physics A*, Vol. 120, No. 1, 287–291, 2015.
6. Zhang, X. and Y. Wu, "Effective medium theory for anisotropic metamaterials," *Scientific Reports*, Vol. 5, No. 1, 1–7, 2015.
7. Li, Y. F., J. Q. Zhang, S. B. Qu, J. F. Wang, L. Zheng, H. Zhou, Z. Xu, and A. X. Zhang, "Wide-band circular polarization-keeping reflection mediated by metasurface," *Chinese Physics B*, Vol. 24, No. 1, 014202, 2015.
8. Li, Y., J. Zhang, S. Qu, J. Wang, H. Chen, Z. Xu, and A. Zhang,"Wideband radar cross section reduction using two-dimensional phase gradient metasurfaces," *Applied Physics Letters*, Vol. 104, No. 22, 221110, 2014.
9. Dai, H., Y. Zhao, H. Li, J. Chen, Z. He, and W. Qi, "An ultra-wide band polarization-independent random coding Metasurface for RCS reduction," *Electronics*, Vol. 8, No. 10, 1104, 2019.
10. Ali, L., Q. Li, T. Ali Khan, J. Yi, and X. Chen, "Wideband RCS reduction using coding diffusion metasurface," *Materials*, Vol. 12, No. 17, 2708, 2019.
11. Chen, K., L. Cui, Y. Feng, J. Zhao, T. Jiang, and B. Zhu, "Coding metasurface for broadband microwave scattering reduction with optical transparency," *Optics Express*, Vol. 25, No. 5, 5571–5579, 2017.
12. Ameri, E., S. H. Esmaeli, and S. H. Sedighy, "Ultra wideband radar cross section reduction by using polarization conversion metasurfaces," *Scientific Reports*, Vol. 9, No. 1, 1–8, 2019.
13. Lin, B. Q., X. Y. Da, J. L. Wu, W. Li, Y. W. Fang, and Z. H. Zhu, "Ultra-wideband and high-efficiency cross polarization converter based on anisotropic metasurface," *Microwave and Optical Technology Letters*, Vol. 58, No. 10, 2402–2405, 2016.
14. Fang, C., Y. Cheng, Z. He, J. Zhao, and R. Gong, "Design of a wideband reflective linear polarization converter based on the ladder-shaped structure metasurface," *Optik*, Vol. 137, 148–155, 2017.
15. Mei, Z. L., X. M. Ma, C. Lu, and Y. D. Zhao, "High-efficiency and wide-bandwidth linear polarization converter based on double U-shaped metasurface," *Aip Advances*, Vol. 7, No. 12, 125323, 2017.
16. Zhao, J. C. and Y. Z. Cheng, "Ultra-broadband and high-efficiency reflective linear polarization convertor based on planar anisotropic metamaterial in microwave region," *Optik*, Vol. 136, 52–57, 2017.
17. Zhang, L., P. Zhou, H. Lu, L. Zhang, J. Xie, and L. Deng, "Realization of broadband reflective polarization converter using asymmetric cross-shaped resonator," *Optical Materials Express*, Vol. 6, No. 4, 1393–1404, 2016.
18. Zhang, L., P. Zhou, H. Chen, H. Lu, J. Xie, and L. Deng, "Broadband and wide-angle reflective polarization converter based on metasurface at microwave frequencies," *Applied Physics B*, Vol. 120, No. 4, 617–622, 2015.
19. Tiwari, P., S. K. Pathak,, V. P. A. V. Siju, and A. Sinha, "X-band Γ-shaped anisotropic metasurface-based perfect cross-polarizer for RCS reduction," *Journal of Electromagnetic Waves and Applications*, Vol. 34, No. 7, 894–906, 2020.
20. Han, T., K. Wen, Z. Xie, and X. Yue, "An ultra-thin wideband reflection reduction metasurface based on polarization conversion," *Progress In Electromagnetic Research*, Vol. 173, 1–8, 2022.
21. Ahmad, T., A. A. Rahim, R. M. H. Bilal, A. Noor, H. Maab, M. A. Naveed, et al., "Ultrawideband cross-polarization converter using anisotropic reflective metasurface," *Electronics*, Vol. 11, No. 3, 487, 2022.